Materials Science & Engineering A 743 (2019) 811–823

Contents lists available at ScienceDirect

Materials Science & Engineering A

journal homepage: www.elsevier.com/locate/msea

Stress state-dependent mechanics of additively manufactured 304L stainless steel: Part 1 – characterization and modeling of the effect of stress state and texture on microstructural evolution

Zhuqing Wang[a], Allison M. Beese[a,b,*]

[a] Department of Materials Science and Engineering, Pennsylvania State University, University Park, PA 16802, United States
[b] Department of Mechanical Engineering, Pennsylvania State University, University Park, PA 16802, United States

ARTICLE INFO

Keywords:
Additive manufacturing
Iron alloys
Phase transformation
Multiaxial stress state
Crystallographic texture

ABSTRACT

The effect of stress state and crystallographic texture on strain-induced martensitic transformation kinetics in 304L stainless steel (SS304L) components made by additive manufacturing were investigated. Mechanical tests under uniaxial tension, uniaxial compression, and pure shear were performed. Experimental results showed that the rate of strain-induced martensitic phase transformation, with respect to plastic strain, was highest under uniaxial compression, followed by uniaxial tension, and lowest under pure shear. The higher rate of phase transformation under uniaxial compression than tension in the additively manufactured SS304L contradicts the trends often, but not always, observed in texture-free conventionally processed austenitic stainless steels. The combined effects of stress state, crystallographic texture, and chemistry were studied, for the first time, to develop a new strain-induced martensitic phase transformation kinetics equation for additively manufactured SS304L that captures the microstructural evolution as a function of plastic strain and these factors.

1. Introduction

Laser-based directed energy deposition (DED) is an additive manufacturing (AM) technique that enables the fabrication of near-net shape 3D components from powder feedstock. During this process, a laser beam creates a melt pool in the material beneath it and the powder is delivered, through nozzles, into the melt pool. As the laser advances, the melt pool rapidly solidifies and fuses to the material below [1–3]. One advantage of AM over traditional fabrication methods is its ability to fabricate complex shaped components [4,5]. When a complex shaped component is subjected to load in a structural application, each location within the component may be subjected to a different stress level and multiaxial stress state. However, thus far, for additively manufactured components, only mechanical properties under uniaxial tension and compression have been reported in the literature [6–17], which is insufficient for describing the mechanical behavior, namely deformation and failure behavior, of the components under realistic multiaxial stress states.

In this study, the deformation-induced, or strain-induced, phase transformation of AISI type 304L austenitic stainless steel (SS304L) fabricated using DED AM was investigated. Deformation induced phase transformation from face-centered cubic (fcc) austenite to body-centered cubic (bcc) α' martensite results in an increase in macroscopic strain hardening rate over that of pure austenite [18–28]. In the strain-induced phase transformation, austenite transforms to α' martensite through two possible pathways [21,29,30]. In the first pathway, austenite first transforms to hexagonal close-packed (hcp) ε martensite, which then transforms to α' martensite. A stacking fault changes the stacking sequence of the {111} planes in austenite from ABCABC to ABABAB, which is the stacking sequence in an hcp structure [31]. Overlapping stacking faults act as nucleation sites for hcp ε martensite, the intersections of which serve as nucleation sites for bcc α' martensite [21,31–33]. In the second pathway, austenite directly transforms to α' martensite [29,30]. The volume fraction of strain-induced α' martensite as a function of plastic strain depends on temperature, chemical composition, texture, strain, strain rate, and stress state [19,22,23]. Previous literature has investigated the effect of these factors on phase transformation independently, but has not studied the combined effects of these factors [24,34–45].

The chemical composition dictates the stacking fault energy (SFE) of austenite, which in turn influences the propensity for strain-induced martensitic transformation kinetics [31]. Alloying elements that increase the SFE of austenite (e.g., carbon, nitrogen, chromium, nickel, silicon, manganese, and molybdenum) decrease the width of stacking

* Corresponding author at: Department of Materials Science and Engineering, Pennsylvania State University, University Park, PA 16802, United States.
E-mail address: amb961@psu.edu (A.M. Beese).

https://doi.org/10.1016/j.msea.2018.11.094
Received 20 September 2018; Received in revised form 17 November 2018; Accepted 19 November 2018
Available online 23 November 2018
0921-5093/

faults, reducing the number of nucleation sites for strain-induced martensite, and increase austenite stability [19,31,46–48]. Rafi et al. [49] investigated the effect of nitrogen and argon atmospheres on the microstructure of additively manufactured 17-4 PH stainless steel. Their results showed that when built in a nitrogen atmosphere, parts consisted of a mixture of austenite (50–75 vol%) and α' martensite (25–50 vol%), but when built in argon, consisted of primarily α' martensite (92 vol%), indicating that nitrogen stabilized austenite. A previous study by the authors on SS304L fabricated using DED AM showed that in walls made from 100 vol% SS304L powder that was gas atomized in nitrogen, the austenite was stable, and did not transform to α' martensite with plastic deformation. Mixing pure iron powder with the gas atomized SS304L powder to fabricate new walls resulted in the decreased stability of austenite and the activation of strain-induced martensitic transformation in these additively manufactured walls with modified composition [50,51].

In additive manufacturing of stainless steel, columnar austenite grains grow along the maximum thermal gradient during deposition, which can potentially result in a preferred crystallographic texture in these components [52,53]. Texture in austenitic stainless steels may significantly impact strain-induced martensitic transformation, because the mechanical driving force for phase transformation depends on the orientation of austenite grains [35–37,45]. Creuziger et al. [45] computed the driving force for textured TRansformation Induced Plasticity (TRIP) steels under uniaxial tension, uniaxial compression, plane strain tension, equi-biaxial tension, equi-biaxial compression, pure shear, deep drawing, and extrusion, using a criterion derived from Schmid's law. They concluded that polycrystalline TRIP steels with a predominant $\{110\}<1\bar{1}2>$ texture (referred to as brass) or $\{112\}<11\bar{1}>$ texture (referred to as copper) had lower driving forces, and therefore, required higher applied stresses for phase transformation, than steels with $\{001\}<100>$ texture (referred to as cube), under all the stress states studied. Similarly, Knijf et al. [37] predicted the driving force for strain-induced martensitic transformation, using the work criterion in [45], in a low carbon polycrystalline steel subjected to uniaxial tension, and showed that materials with cube and $\{110\}<001>$ (referred to as Goss) texture had higher driving forces for phase transformation under uniaxial tension than those with brass and copper textures. Hilkhuijsen et al. [35,36] investigated strain-induced martensitic transformation in both untextured and highly textured stainless steels under uniaxial tension. Their results showed the evolution of α' martensite content with respect to plastic strain was independent of orientation in untextured specimens. However, for specimens with a mixture of copper and Goss textures, more α' martensite was formed in textured specimens whose loading axes were along the rolling direction than along the transverse direction.

Stress state also impacts strain-induced martensitic transformation in steels with retained austenite, but the experimental results reported in the literature are inconsistent as highlighted in Table 1 [24,34,38–44,54,90,91]. These inconsistencies may stem from differences in crystallographic texture of samples, or pollution of experimental measurements due to surface effects and limitations of the measurement method, or the effect of elastic strain on magnetic permeability measurements as discussed in Section 3.1.

As experimental investigations are contradictory, the proposed equations to describe the transformation kinetics are also diverse. Olson and Cohen [23] proposed a transformation kinetics equation that captured the effect of plastic strain and temperature on annealed 304 stainless steel under uniaxial tension [19]. Stringfellow et al. [22] expanded this equation by incorporating the effect of stress triaxiality, proposing that the rate of strain-induced martensitic transformation increases with stress triaxiality. Their equation was based on experimental data under uniaxial tension and compression obtained by Young [55]. Kosarchuk and Lebedev [41,56] studied strain-induced martensitic transformation kinetics in austenitic stainless steel 18–10 subjected to uniaxial tension, uniaxial compression, torsion, and equi-biaxial tension. Their experimental results indicated that stress triaxiality was not the only factor that affected martensitic transformation, and they suggested that the phase transformation appeared to also depend on the Lode angle parameter. Beese and Mohr [24] proposed a strain-induced martensitic transformation equation for austenitic stainless steel that fully incorporated the effect of stress state, by including the dependence on stress triaxiality and Lode angle parameter in addition to plastic strain. Their data under uniaxial tension, uniaxial compression, plane strain tension, and equi-biaxial tension, and proposed and calibrated transformation kinetics equation, for untextured austenitic stainless steel 301LN showed that the rate of transformation with respect to plastic strain increased with increasing stress triaxiality and Lode angle parameter.

The strain-induced martensitic phase transformation kinetics in austenitic stainless steels with little to no texture under various stress states have been investigated extensively [24,34,38–43,55–58], but multiaxial stress states investigations on textured austenitic stainless steels have not yet been reported. The aim of the present study was to investigate the effect of stress state on strain-induced martensitic phase transformation in textured SS304L, with two different chemistries, deposited by DED AM. The evolution of α' martensite volume fraction with plastic deformation was quantified using *in situ* magnetic permeability and neutron diffraction measurements during mechanical tests under uniaxial tension, pure shear, and uniaxial compression. For the first time, a strain-induced martensitic phase transformation kinetics equation describing the combined effects of stress state, texture, and chemistry on the α' martensite volume fraction as a function of equivalent plastic strain is proposed. This model was calibrated using novel experiments on additively manufactured SS304L. This newly developed transformation kinetics equation can be used to describe the evolution of microstructural phase content, which is required for the development of a physically-based plasticity model, as described in the companion paper [59], that can describe the constitutive behavior of textured austenitic stainless steels.

2. Materials

Two 140 mm long × 104 mm tall × 14 mm thick walls were deposited by laser-based DED AM onto annealed 304L stainless steel substrates (ASTM A479 standard [60]) using mixtures of pre-alloyed SS304L powder and pure iron powder. The pre-alloyed SS304L powder was fabricated by gas atomization in nitrogen (Carpenter Powder Products, Corp.) with the elemental composition shown in Table 2. The iron powder was fabricated by hydrogen reduction (Atlantic Equipment Engineers) and had a purity of 99.8%. Both SS304L powder and iron powder were sieved to a mesh size of + 325/-100, corresponding to powder diameters between 45 μm and 145 μm. In order to isolate the effect of powder chemistry on the strain-induced austenite-to-martensite transformation, the same processing parameters were used to fabricate the two walls. One wall was built using 80 vol% SS304L powder mixed with 20 vol% iron powder, denoted as the 80% SS304L wall, and the other was built using 90 vol% SS304L powder mixed with 10 vol% iron powder, denoted as the 90% SS304L wall.

The two walls were fabricated using a custom-built DED system with a chamber purged with ultra-high purity argon to reduce oxygen contamination. An ytterbium fiber laser (IPG Photonics® YLR-12000-L) with a wavelength in the range of 1070 and 1080 nm was used at a laser power of 2 kW and a scanning speed of 10.6 mm/s for material deposition. The powder was delivered to the melt pool using a custom-designed four-nozzle delivery system at a powder flow rate of 15.5 g/min. The substrate was placed about 10 mm below the nozzles, corresponding to a defocused position of the laser beam, resulting in a beam diameter of 4 mm. The walls were fabricated by depositing a 140 mm long bead of material corresponding to the length of the wall, with 6 adjacent laser passes, and a hatch spacing of 2.5 mm, resulting in a wall thickness of 14 mm. The vertical layer thickness was about 1.1 mm.

Table 1
Comparison of findings on the effect of stress state on strain-induced phase transformation in existing literature. The relative amounts of newly formed α' martensite are represented by the number of plus symbols.

Reference	Material	Processing condition	Uniaxial tension	Uniaxial compression	Shear	Equi-biaxial tension	Plane strain tension	Texture	α'martensite measurement technique
Cina, 1954 [34]	Steels containing 18–25% chromium and 8–12% nickel	NR[a]	+ +	+				NR	X-ray diffraction, magnetic balance
Powell et al., 1958 [38]	301 and 304 stainless steels	NR	+ +	+	+			NR	Density measurement
Hecker et al. and Murr et al., 1982 [39,40]	304 stainless steel	Annealed	+			+ +		NR	Magnetic permeability, magnetic saturation
Young, 1988 [55]	Steels containing 16% chromium and 10% nickel	NR	+ +	+				NR	Magnetic moment
Kosarchuk et al., 1989 [41]	Steels containing 16% chromium and 10% nickel	Annealed	+ +			+		NR	X-ray diffraction
Demania, 1995 [87]	304L stainless steel	Cold rolled	+ +				+	NR	Magnetic moment
Miller and McDowell, 1996 [88]	304L stainless steel	Annealed		+ +	+			NR	Magnetization studies
Iwamoto et al.,1998 [42]	304 stainless steel	Annealed	+ + (strain < 20%) + (strain > 20–40%)	+(strain < 20%) + + (strain > 20–40%)				NR	Scanning electron microscopy
Lebedev and Kosarchuk, 2000 [56]	Steels containing 18% chromium and 10% nickel	Hot rolled	+ + +	+	+ +			NR	X-ray diffraction, optical microscopy
Shin et al., 2003 [89]	304 stainless steel	Annealed	+	+ +	+ + +			NR	Magnetic permeability
Yu et al., 2006 [43]	TRIP 600 steel	Cold rolled	+			+ +	+ + +	NR	X-ray diffraction
Perdahcioglu et al., 2008 [90]	A564 stainless steel	NR			+		+ +	NR	Magnetic sensor
Nanga et al., 2009 [91]	301LN and 201 stainless steels	Cold rolled and annealed	+ + +		+	+ + +	+ +	NR	Magnetic saturation
Beese and Mohr, 2011 [24]	301LN stainless steel	Temper rolled	+ + + +	+		+ +	+ + +	Negligible	Magnetic permeability
Han and Yuan, 2013 [54]	304 stainless steel	Annealed	+ +	+				NR	Magnetic permeability
Kim et al., 2015 [44]	TRIP 718 steel	NR	+		+ +		+ + +	NR	Magnetic permeability
Wang and Beese, current study	80% SS304L 90% SS304L	Additively manufactured	+ +	+ + +	+			{111} $<1\bar{1}0>$	Magnetic permeability

[a] NR in the table indicates not reported.

Table 2
Elemental composition (wt%) of the pre-alloyed SS304L powder and the additively manufactured 80% and 90% SS304L walls.

	C	N	Si	Mn	Cr	Ni	Mo	Fe
SS304L powder	0.01	0.08	0.50	1.50	19.0	10.3	0.01	Balance
80% SS304L wall	0.01	0.09	0.63	1.27	16.73	9.08	0.05	Balance
90% SS304L wall	0.01	0.09	0.70	1.31	17.05	9.47	0.05	Balance

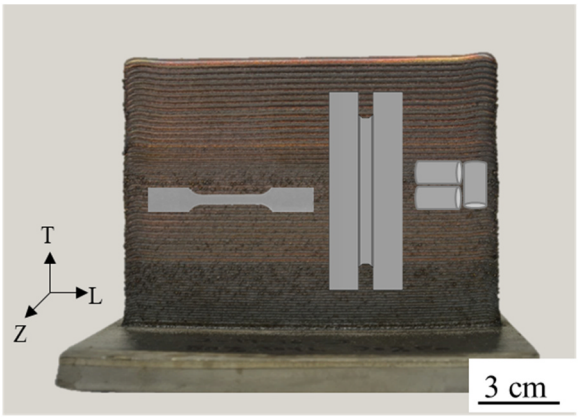

Fig. 1. Photograph of the additively manufactured wall with a schematic representation of the positions from which uniaxial tension, shear, and uniaxial compression samples were extracted. Here, L is the longitudinal direction, T is the transverse, or build direction, and z is the thickness direction.

These processing parameters were selected based on a previous study by the authors, for which these parameters resulted in fully-dense walls [50].

3. Experimental procedure

3.1. Uniaxial tension

Uniaxial tension specimens with gauge dimensions of 21.5 mm length, 4 mm width, and 1.5 mm thickness, in accordance with ASTM E8 [61], were extracted from both walls, along the longitudinal direction, using wire electrical discharge machining (EDM), as shown in Fig. 1. By extracting such thin samples, the residual stresses, which existed in the as-built walls, were assumed to be relieved [62]. As shown in previous studies by the authors, location-dependent martensitic transformation and mechanical properties were found along the vertical build direction of the additively manufactured SS304L walls. These were determined to be derived from variations in chemical composition with vertical position due to preferential elemental vaporization with height, and variations in austenite grain size with vertical position due to heat accumulation with height [50,51]. Therefore, to eliminate the impact of spatial variations in chemistry and grain size in this study, at least three samples were extracted from each wall such that the gauge centers of all specimens were at the same height, about 40 mm away from the bottom of each wall. Energy dispersive spectroscopy line scans were performed on a longitudinal specimen to confirm that no significant chemical variations were present along the length direction of the wall. Lack-of-fusion pores perpendicular to the vertical build direction were observed in the two walls in a previous study by the authors, which lead to early failure, significantly reducing the potential for strain-induced martensitic transformation when applied tension is along the build direction [51]. Therefore, only longitudinal tension specimens were examined in the current study.

The amount of strain-induced martensite, with increased deformation, in the test specimens was quantified by magnetic permeability measurements using a feritescope (Fisher Feritescope FMP 30), which incorporates contributions from all ferromagnetic phases present. The as-deposited SS304L contained paramagnetic austenite and ferromagnetic ferrite (less than 2 vol%). When SS304L is subjected to plastic deformation, strain-induced martensitic transformation may occur, while the ferrite will not undergo a solid-state phase transformation. As ε martensite is paramagnetic, any increase in magnetic permeability corresponds to the increase in α' martensite volume fraction [22,63–65].

An important experimental consideration when measuring α' martensite using magnetic permeability is the fact that when elastically deformed under tension, the magnetic permeability of ferromagnetic materials is reduced due to the rotation and reorientation of magnetic domains with applied stress. This is referred to as negative magnetostriction or the Villari effect [66]. Therefore, magnetic permeability measurements must be conducted on macroscopically stress-free specimens to reduce the influence of the Villari effect on the feritescope measurements [67]. In this study, periodic loading/unloading tests were used to quantify the evolution of α' martensite using magnetic permeability as the measurement method. Specifically, the uniaxial tension specimens were loaded to 7% engineering strain, unloaded to zero stress, at which point the magnetic permeability was measured, and reloaded to an additional 7% engineering strain. The corresponding true stress-strain curves for periodic loading/unloading tests are given in [51]. This loading, unloading, and measurement procedure was used to ensure that the samples were macroscopically stress-free for the measurement of α' martensite.

Uniaxial tension tests with *in situ* feritescope measurements were performed using an electromechanical testing frame (Instron 4202, 10 kN load cell). Each specimen was loaded under displacement control at a strain rate of 1.2×10^{-3}/s. Digital image correlation (DIC) was used to compute strains (Vic2D, Correlated Solutions). For DIC, a white background and a random black speckle pattern were painted onto the specimen gauge region before each test. A digital camera (Point Grey GRAS-50S5M-C) recorded images of the deforming gauge region at a rate of 1 Hz. The surface deformation fields were computed from the digital images using a cubic B-spline interpolation algorithm with a subset of 21 pixels and step size of 5 pixels, resulting in a virtual strain gauge size of 56 pixels or 1.5 mm [68]. A 21 mm long vertical virtual extensometer was used to compute axial strain in each specimen.

In order to measure the evolution of α' martensite content during loading/unloading tests, the feritescope probe was held perpendicular to the gauge of specimen and in direct contact with surface during the test. The feritescope measures the magnetic permeability of a finite volume of material, which is approximately a cylinder measuring 5 mm in diameter and 2 mm in depth [69]. If the width of the sample decreases below 4 mm, or the thickness decreases below 2 mm, the output of the feritescope, $S_{Fe,m}$, must be corrected by a width correction factor, a, and a thickness correction factor, b [67,69]. The volume fraction of α' martensite, c, can be computed from the feritescope output as [67]:

$$c = kab\Delta S_{\mathrm{Fe},m} = kab(S^{\,t}_{\mathrm{Fe},m} - S^{\,0}_{\mathrm{Fe},m}) \quad (1)$$

where $S^{t}_{Fe,m}$ is the feritescope reading (units of vol% ferrite), which is indicative of the volume fraction of ferromagnetic material; $S^{0}_{Fe,m}$ is the measured initial volume fraction of ferromagnetic material in the undeformed specimen; and $k = 1.8$ is the conversion factor from the feritescope output to the volume fraction of α' martensite [51].

3.2. Pure shear

Specimens with a reduced thickness gauge section, shown in Fig. 2 [70], were used to perform tests under pure shear. With this geometry, the gauge length along the x direction is 10 times larger than the height in the y direction, resulting in a nearly zero strain along the x direction, or a plane strain condition. The gauge thickness along the z direction is 0.5 mm, resulting in the relieving of residual stresses upon extraction of

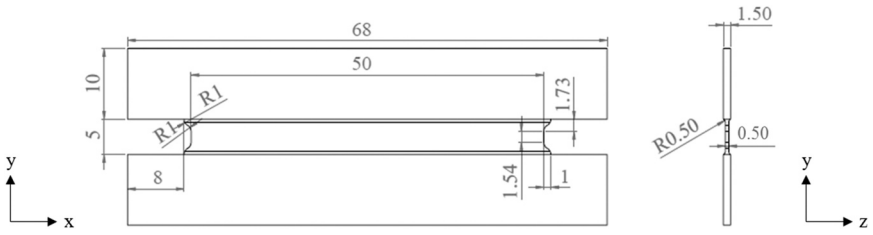

Fig. 2. Specimen geometry for pure shear tests (units: mm), adapted from [70].

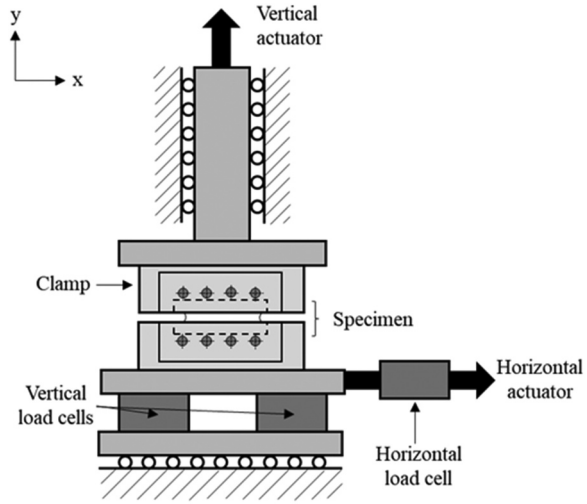

Fig. 3. Schematic of the dual actuator hydraulic test frame for multiaxial testing.

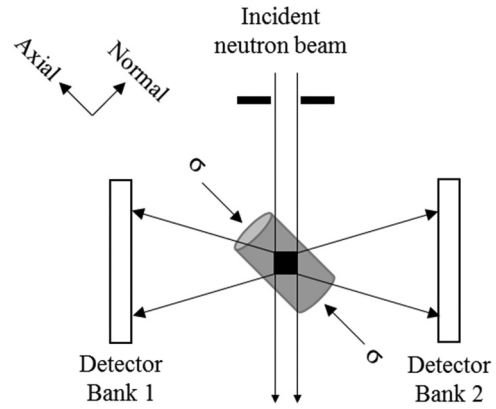

Fig. 4. Schematic of a compression test with *in situ* neutron diffraction, in which diffraction patterns along axial and normal directions were collected.

these thin specimens [62]. Three shear specimens were extracted using wire EDM from each additively manufactured wall such that the gauge centers were 40 mm from the bottom of the walls.

Shear tests were performed using a custom-built dual actuator hydraulic test frame (MTS Systems Corp.) shown schematically in Fig. 3. In this system, the vertical force is measured by two 100 kN load cells and the horizontal force by a 50 kN load cell. In pure shear tests, displacement control was used to apply a horizontal strain rate of 1.3×10^{-3}/s, while the vertical force was set to zero, which provides a pure shear loading state [70]. The evolution of α' martensite content with respect to plastic strain in the shear tests was measured using magnetic permeability measurements during periodic loading/unloading tests, in which increments of 6% horizontal engineering strain were used with a procedure similar to that for uniaxial tension described in Section 3.1. DIC was used to calculate strains in the gauge region of each specimen. A subset of 25 pixels and a step size of 6 pixels were used, resulting in a virtual strain gauge size of 67 pixels or 0.8 mm [68]. The vertical and horizontal strains were measured using 3 mm long virtual vertical and horizontal extensometers.

3.3. Uniaxial compression

Cylindrical specimens measuring 8 mm in diameter and 16 mm long were used to characterize the compressive behavior of the additively manufactured material. Three longitudinal and three transverse specimens were extracted, using wire EDM, from a height of 40 mm from the bottom of each wall, as shown in Fig. 1. No notable residual stresses were found in the specimens. Monotonic uniaxial compression tests were conducted at a strain rate of 1.5×10^{-5}/s with *in situ* neutron diffraction on the VULCAN instrument at the Spallation Neutron Source at Oak Ridge National Laboratory [71–73]. The VULCAN instrument has two detector banks that collected diffraction patterns from grains whose *hkl*-specific lattice planes were perpendicular to the axial and normal directions, as schematically shown in Fig. 4. The d-spacings and integrated intensities of *hkl*-specific lattice planes from austenite (γ, fcc) and strain-induced martensite (α', bcc) were measured to compute the volume fractions of austenite and α' martensite using the internal standard method described below [74].

The intensity of an *hkl*-specific peak in austenite, $I_{hkl,\gamma}$, is expressed as:

$$I_{hkl,\gamma} = \frac{K_e K_{hkl,\gamma} V_\gamma}{\left(\frac{\mu}{\rho}\right)_m} \tag{2}$$

where K_e is an experimental system constant; V_γ is the volume fraction of austenite; $\left(\frac{\mu}{\rho}\right)_m$ is the mass absorption coefficient in SS304L; and $K_{hkl,\gamma}$ is a constant for an *hkl*-specific peak in austenite, given as:

$$K_{hkl,\gamma} = \frac{1}{v_\gamma^2} M_{hkl,\gamma} |F_{hkl,\gamma}|^2 L_{hkl,\gamma} O_{hkl,\gamma} \tag{3}$$

where $M_{hkl,\gamma}$ is the multiplicity, which is the number of identically spaced planes in a *hkl*-specific family; v_γ is the volume of a unit cell of austenite; $F_{hkl,\gamma}$ is the structure factor; $L_{hkl,\gamma}$ is the Lorentz factor, which equals to $d_{hkl,\gamma}{}^4 \sin\theta$, in which θ is 45° in the neutron diffraction setup and $d_{hkl,\gamma}$ is the lattice spacing; and $O_{hkl,\alpha}$ is the texture correction factor.

From Eq. (2), the internal standard method gives that the relative volume fractions of the two phases are:

$$\frac{V_\gamma}{V_{\alpha'}} = \frac{I_{hkl,\gamma} K_{hkl,\alpha'}}{I_{hkl,\alpha'} K_{hkl,\gamma}} \tag{4}$$

where $V_{\alpha'}$ is the volume fraction of α' martensite; $K_{hkl,\alpha'}$ is a constant for an *hkl*-specific peak in α' martensite; and $I_{hkl,\alpha'}$ is an *hkl*-specific peak intensity in α' martensite.

To confirm the internal standard method measurements, the phase fractions were also calculated using Rietveld refinement for a transverse compression specimen from the 90% SS304L wall. For this analysis, the General Structural Analysis Software (GSAS), which takes into account sample texture, was used to determine the phase fractions [75,76].

3.4. Magnetic saturation

The most accurate method for quantifying the volume fraction of a ferromagnetic phase in a sample is through magnetic saturation measurements, which are not affected by the size, texture, or surface preparation of the sample, nor elastic strains within the sample [67]. In this method, a ferromagnetic specimen is placed in a magnetic field, and it becomes magnetized as the magnetic dipoles in the sample align parallel to the applied field. The magnetic induction of the specimen increases with the strength of the applied magnetic field until it reaches a saturation value. As the saturation magnetization of α' martensite is 154 emu/g [77], the volume fraction of ferromagnetic material in the samples equals the saturation magnetization of the sample divided by 154 emu/g. In order to validate the α' martensite content determined by magnetic permeability measurements, magnetic saturation measurements were performed using a sigmameter (SETARAM Sigmameter D6025) on two deformed specimens with different amounts of equivalent plastic strain. The α' martensite content was obtained by subtracting the volume fraction of ferrite, which was under 2% in each specimen, from the computed volume fraction of ferromagnetic material. The α' martensite volume fraction measured by the feritescope was compared to that measured by magnetic saturation (via a sigmameter) as shown in Fig. 5. The 1:1 ratio of these measurements indicates that the width- and thickness-corrected magnetic permeability measurements, and the conversion factor of $k = 1.8$ in Eq. (1) are accurate.

3.5. Texture determination

In the present study, inverse pole figures were used to represent the crystallographic texture. The integrated peaks of (111), (200), (220), (311), (222), (331), (420), and (531) from austenite in a transverse compression specimen during plastic deformation were obtained from *in situ* neutron diffraction patterns. Based on the experimental data, a quasi-Monte Carlo method coupled with the barycentric interpolation was used to determine the inverse pole figures [78]. Reference samples made from scrap powder detached from a similar material plate were used to normalize the intensities of diffraction peaks.

3.6. Chemical and microstructural analysis

The elemental compositions of the as-deposited material from both walls, 40 mm above the baseplate, were measured (Element Materials Technology, Newtown, PA) as shown in Table 2. The carbon and sulfur contents were measured using combustion testing, and the nitrogen content was measured using inert gas fusion (ASTM E1019 [79]). The remaining elements were measured using optical emission spectrometry (ASTM E1086 [80]).

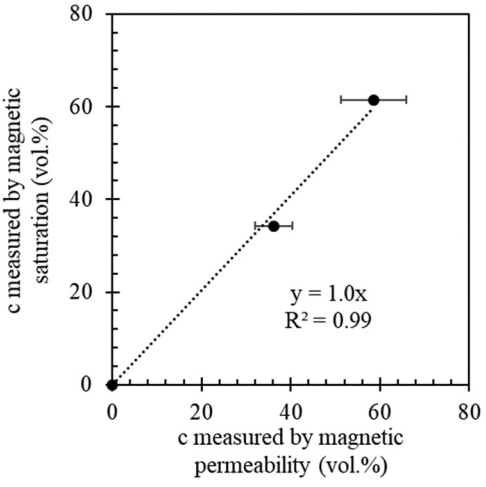

Fig. 5. Volume fraction of α' martensite, *c*, measured by magnetic saturation versus *c* measured by magnetic permeability.

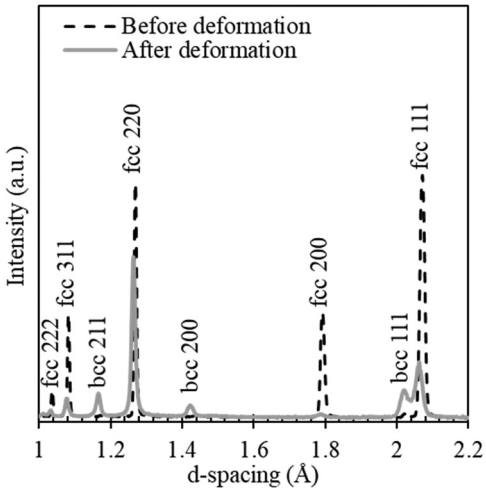

Fig. 6. Neutron diffraction patterns, along the loading direction of a transverse specimen from the 90% SS304L wall, before and after uniaxial compression to 27% engineering strain.

The microstructure of a representative uniaxial tension specimen from the 90% SS304L wall was characterized using electron backscatter diffraction (EBSD; Oxford Nordlys Max2). Specimens were polished using standard metallurgical techniques with a final polishing step using 0.05 μm colloidal silica for grain observation.

4. Results and discussion

4.1. Effect of direction on strain-induced martensitic transformation

In uniaxial compression tests, the evolution of α' martensite content with respect to plastic strain was computed using the internal standard method from neutron diffraction (Eqs. (2)–(4)). Fig. 6 shows neutron diffraction patterns from a transverse cylindrical specimen from the 90% SS304L wall before and after 27% plastic deformation. The volume fraction of ferromagnetic material in the as-built sample was measured to be below 2%, as demonstrated by the low intensities of bcc peaks in the diffraction pattern before plastic deformation in Fig. 6. The increase in bcc peak intensities after plastic deformation is the result of newly formed strain-induced α' martensite. To quantify the amount of α' martensite formed using the internal standard method, the (220) and (200) peaks from fcc austenite, and (211) and (200) peaks from bcc α' martensite were used, per ASTM E975 [81]. As a validation of this approach, the α' martensite content evolution in a 90% SS304L transverse compression specimen computed using the internal standard method is compared to that computed using Rietveld refinement in Fig. 7. The good agreement between the two curves confirms the accuracy of the internal standard method for calculating α' martensite content under uniaxial compression.

Fig. 8 shows the volume fraction of α' martensite as a function of plastic strain in longitudinal and transverse specimens from the 90% SS304L wall under uniaxial compression, showing that there is no notable anisotropy in the strain-induced martensitic transformation kinetics of this material.

4.2. Effect of stress state and texture on strain-induced martensitic transformation

Strain-induced martensite evolution curves for longitudinal specimens from the two walls under uniaxial tension, pure shear, and uniaxial compression are given in Fig. 9. As shown in Fig. 9, in a single

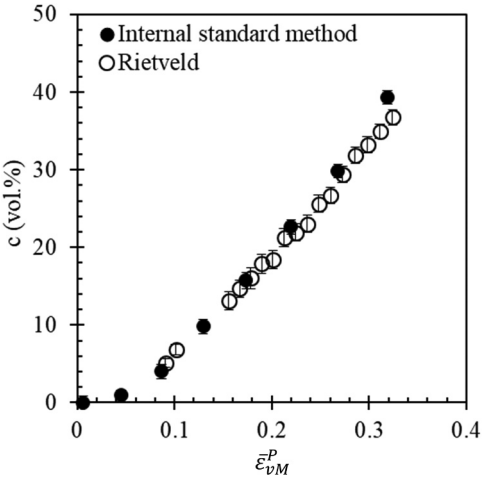

Fig. 7. Volume fraction of α' martensite, *c*, as a function of von Mises equivalent plastic strain, $\bar{\varepsilon}^P_{vM}$, determined by the internal standard method and Rietveld refinement in a transverse compression specimen from the 90% SS304L wall.

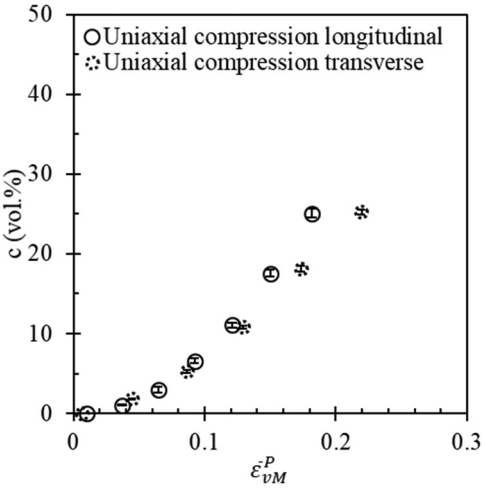

Fig. 8. Volume fraction of α' martensite, *c*, as a function of von Mises equivalent plastic strain, $\bar{\varepsilon}^P_{vM}$, for longitudinal and transverse specimens from the 90% SS304L wall under uniaxial compression.

wall, the slope of the austenite-to-α' martensite transformation kinetics curve, or the rate of martensitic transformation with respect to plastic strain, is the highest under uniaxial compression, followed by uniaxial tension, and lowest under pure shear. The finding of a higher rate of transformation under compression than tension in additively manufactured SS304L contradicts most of the data on phase transformation in texture-free materials.

Representative EBSD maps from the 90% SS304L wall are given in Fig. 10. As shown in Fig. 10, columnar austenite grains tend to grow along the vertical build direction, or along the maximum thermal gradient during deposition, which may result in a preferred crystallographic texture in the component [52,53,82]. As shown in the inverse pole figures of a transverse compression specimen in the present study in Fig. 11, the predominant texture of the walls studied here was $\{111\} < 1\bar{1}0 >$, in which $< 1\bar{1}0 >$ was parallel to the transverse (build) direction within the wall, and $< 111 >$ was parallel to the longitudinal direction within the wall. The predominant texture did not change after plastic deformation (see Fig. 11). It has been shown previously that texture in austenitic stainless steels affects the austenite-to-α' martensite transformation under uniaxial tension [35,36].

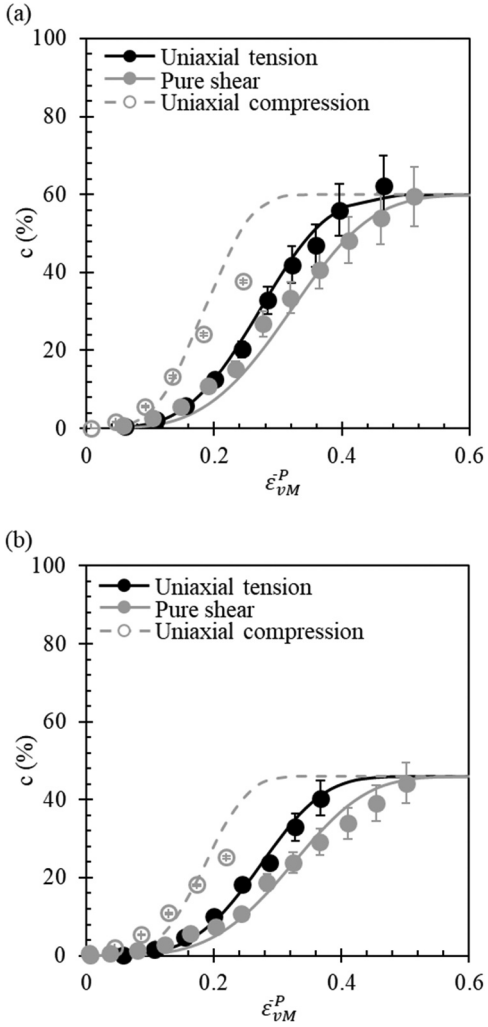

Fig. 9. Volume fraction of α' martensite, *c*, as a function of von Mises equivalent plastic strain, $\bar{\varepsilon}^P_{vM}$, in longitudinal specimens from the (a) 80% SS304L wall and (b) 90% SS304L wall under uniaxial tension, pure shear, and uniaxial compression. Symbols correspond to experimental data and lines correspond to the calibrated transformation kinetics equation.

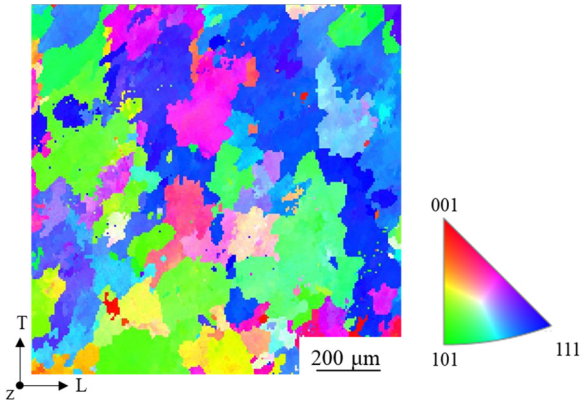

Fig. 10. EBSD map of a cross-section whose normal is parallel to the thickness direction of the 90% SS304L wall. Here, L is the longitudinal direction, T is the transverse, or build direction, and z is the thickness direction. The colors represent *hkl*-specific plane normals coming out of the page.

The strain-induced α' martensite is transformed directly from austenite or from the intermediate ε martensite phase [21,29,30]. There are 24 variants for the austenite-to-α' martensite transformation, and

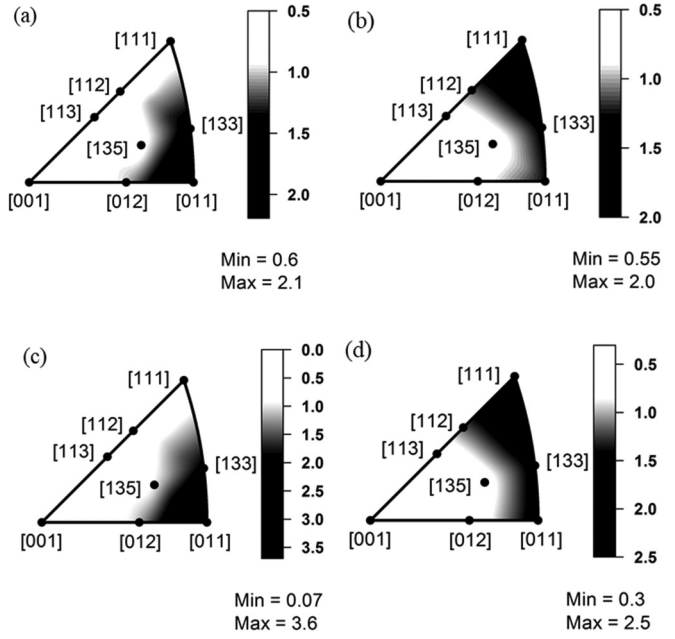

Fig. 11. Inverse pole figures, determined by neutron diffraction, for a transverse compression specimen from the 90% SS304L wall with crystal directions parallel to the (a) loading, or transverse, direction, (b) normal, or longitudinal, direction before plastic deformation, and (c) loading direction, and (d) normal direction after 27% plastic deformation.

12 variants for the austenite-to-ε martensite transformation [83,84]. The driving force of martensitic transformation for the ith variant, w_i, can be calculated by [45]:

$$w_i = \boldsymbol{s_i}\sigma_a\boldsymbol{n_i} \tag{5}$$

where $\boldsymbol{\sigma_a}$ is the applied stress tensor in the coordinate system of an austenite unit cell; $\boldsymbol{n_i}$ is the habit plane normal; and $\boldsymbol{s_i}$ is the shear direction of the ith variant. The driving force is the stress needed for phase transformation from austenite to α' or ε martensite for a single variant. It has a similar mathematical form as the critically resolved shear stress, as Eq. (5) is derived from Schmid's law [85]. The vectors, $\boldsymbol{n_i}$ and $\boldsymbol{s_i}$, correspond to each variant, and in austenite-to-α' martensite transformation, they also depend on the lattice parameters of austenite and α' martensite [83]. Through neutron diffraction, the lattice parameter for fcc austenite was determined to be 0.358 nm, and that for bcc α' martensite, 0.287 nm. An example of $\boldsymbol{n_i}$ and $\boldsymbol{s_i}$ values for one variant, calculated using Eq. (5) and the approach in [45], is (0.585, 0.788, 0.190) [−0.149, 0.161, −0.048] for the austenite-to-α' martensite transformation and (0.144, 0.144, −0.289) [0.577, 0.577, 0.577] for the austenite-to-ε martensite transformation, which match well with the vectors reported in literature [29,30]. The cubic symmetry operator was applied to (0.585, 0.788, 0.190) [−0.149, 0.161, −0.048] to calculate the vectors for the rest of the variants for the austenite-to-α' martensite transformation. The hexagonal symmetry operator was applied to (0.144, 0.144, −0.289) [0.577, 0.577, 0.577] to calculate the vectors for the variants for the austenite-to-ε martensite transformation.

In order to transform the applied stress tensor into the austenite coordinate system (or that of the textured component), the following equation is used:

$$\boldsymbol{\sigma_a} = \boldsymbol{R}\,\boldsymbol{\sigma}\boldsymbol{R}^T \tag{6}$$

where $\boldsymbol{\sigma}$ is the stress tensor in the specimen coordinate system; and $\boldsymbol{R}$ is the rotation matrix given as:

$$\boldsymbol{R} = \begin{bmatrix} \cos\varphi_1 & \sin\varphi_1 & 0 \\ -\sin\varphi_1 & \cos\varphi_1 & 0 \\ 0 & 0 & 1 \end{bmatrix}\begin{bmatrix} 1 & 0 & 0 \\ 0 & \cos\Phi & \sin\Phi \\ 0 & -\sin\Phi & \cos\Phi \end{bmatrix}\begin{bmatrix} \cos\varphi_2 & \sin\varphi_2 & 0 \\ -\sin\varphi_2 & \cos\varphi_2 & 0 \\ 0 & 0 & 1 \end{bmatrix} \tag{7}$$

where φ_1, Φ, and φ_2 are Euler angles between the specimen and austenite coordinate systems.

For a given stress state, the austenite-to-martensite variant with the highest driving force has the highest probability of transformation [35,36,45]. Therefore, the driving force for phase transformation in austenite grains, W, as a function of the three Euler angles, is:

$$W(\varphi_1, \Phi, \varphi_2) = \max\,(w_i(\boldsymbol{\sigma}, \varphi_1, \Phi, \varphi_2)) \tag{8}$$

To compare the driving forces under uniaxial tension, pure shear, and uniaxial compression, for the preferred crystallographic texture seen here, normalized stress states were defined such that the non-dimensional von Mises equivalent stress of each stress state was 1. The resulting stress tensors for uniaxial tension, $\boldsymbol{\sigma_{UT}}$, pure shear, $\boldsymbol{\sigma_{shear}}$, and uniaxial compression, $\boldsymbol{\sigma_{UC}}$, are:

$$\begin{aligned} \boldsymbol{\sigma_{UT}} &= \begin{bmatrix} 1 & 0 & 0 \\ 0 & 0 & 0 \\ 0 & 0 & 0 \end{bmatrix}; \\ \boldsymbol{\sigma_{shear}} &= \begin{bmatrix} 0 & \frac{1}{\sqrt{3}} & 0 \\ \frac{1}{\sqrt{3}} & 0 & 0 \\ 0 & 0 & 0 \end{bmatrix}; \\ \boldsymbol{\sigma_{UC}} &= \begin{bmatrix} -1 & 0 & 0 \\ 0 & 0 & 0 \\ 0 & 0 & 0 \end{bmatrix} \end{aligned} \tag{9}$$

Using Eqs. (5)–(9), the orientation distribution plots of the non-dimensional mechanical driving forces for austenite-to-α' martensite and austenite-to-ε martensite transformations under the three stress states on the section of $\varphi_2 = 45°$ are shown in Figs. 12 and 13. The initial preferred texture for transverse specimens, using the notation of {normal direction} < loading direction >, was $\{111\} < 1\bar{1}0 >$, corresponding to (0°, 55°, 45°). The initial preferred texture for longitudinal specimens was $\{1\bar{1}0\} < 111 >$, corresponding to (35°, 90°, 45°). The non-dimensional mechanical driving forces for specimens with initial preferred textures of (0°, 55°, 45°) and (35°, 90°, 45°) under uniaxial tension, pure shear, and uniaxial compression are given in Table 3. As shown in Table 3, under uniaxial compression, the non-dimensional mechanical driving forces for both martensitic transformations in longitudinal and transverse specimens with the preferred texture in this study are similar. This is consistent with the curves in Fig. 8, which show no notable anisotropy in martensitic transformation. The longitudinal and transverse specimens have different crystallographic textures, but the martensitic transformation kinetics are approximated to be isotropic, as the driving forces for phase transformation, which depend on the combined effects of stress state and texture, are similar for longitudinal and transformation specimens under uniaxial compression. In the longitudinal orientation, compared to the driving force for austenite-to-ε martensite transformation, the driving force for austenite-to-α' martensite transformation is much smaller under uniaxial tension and pure shear, but close under uniaxial compression for the preferred texture seen here. This implies that the austenite-to-ε martensite transformation is dominant under uniaxial tension and pure shear, and both austenite-to-ε martensite and austenite-to-α' martensite transformations may occur under uniaxial compression. The stress state- and texture-dependent phase transformation paths affect the driving force for martensitic transformation. Further work, beyond the scope of this study, is required to determine the driving force for ε martensite-to-α' martensite transformation and the actual phase transformation pathway for materials with texture studied under various stress states.

4.3. Effect of chemistry on strain-induced martensitic transformation

The elemental compositions of the two SS304L walls, given in Table 2, affect the rate, with respect to plastic strain, and saturation

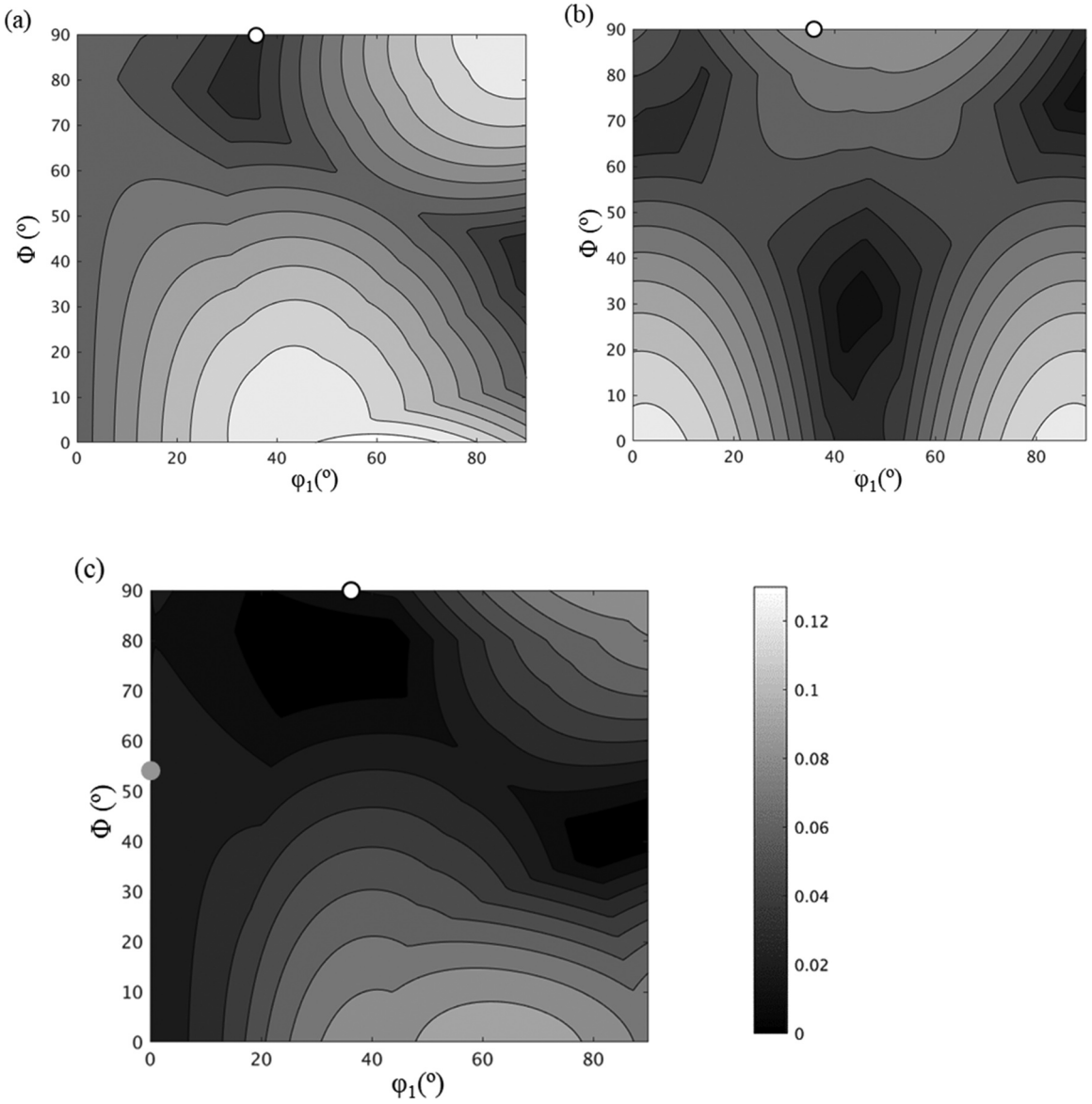

Fig. 12. Orientation distribution plots of non-dimensional mechanical driving force for austenite-to-α' martensite transformation on the section of $\varphi_2 = 45^\circ$ for (a) uniaxial tension, (b) pure shear, and (c) uniaxial compression. The orientations of longitudinal specimens are marked with open symbols at (35°, 90°, 45°). The orientation of the transverse specimen is marked with a solid symbol at (0°, 55°, 45°).

values, of strain-induced martensitic transformation kinetics in the materials, as shown in Fig. 9. Under the same stress state, the slopes and saturation values of the transformation kinetics curves are higher in specimens from the 80% SS304L wall than those from the 90% SS304L wall. With an increase in the volume fraction of iron powder, the relative content of elements that stabilize austenite against the strain-induced transformation to martensite (silicon, manganese, chromium, and nickel) decreases [51]. Therefore, compared to the 90% SS304L wall, austenite is less stable, resulting in a higher rate of transformation to, and a higher saturation value of, α' martensite in the 80% SS304L wall. The effect of chemistry, which was studied in detail in [51], is taken into account in the newly proposed transformation kinetics equation presented in Section 4.4.1.

4.4. Strain-induced martensitic transformation kinetics equation

4.4.1. Existing strain-induced martensitic transformation kinetics equation

Santacreu et al. [86] proposed the following stress state-independent phase transformation kinetics equation to describe the evolution of α' martensite volume fraction as a function of plastic strain in conventionally processed austenitic 301LN stainless steel:

$$\frac{c}{c_{max}} = 1-\exp\{-[D(\bar{\varepsilon}_P)]^n\} \tag{10}$$

where c_{max} is the saturation value of the volume fraction of strain-induced α' martensite that can be transformed from austenite; n and D are material constants; $\bar{\varepsilon}_P$ is the equivalent plastic strain. Here, $\bar{\varepsilon}_P$ is taken to be $\bar{\varepsilon}^P_{vM}$ due to the isotropy of the strain-induced martensitic transformation kinetics (Fig. 8). The parameters n and D describe to the rate of martensitic transformation with respect to plastic strain, where a small value of n and a large value of D correspond to a high rate of phase transformation with respect to plastic strain.

The strain-induced martensitic transformation kinetics curves in the two SS304L walls are affected by stress state, as shown in Fig. 9. Therefore, a stress state-dependent strain-induced martensitic transformation kinetics equation is required. Beese and Mohr [24] expanded the transformation kinetics equation in Eq. (10) by incorporating the effect of stress state, where the stress state can be described by the stress

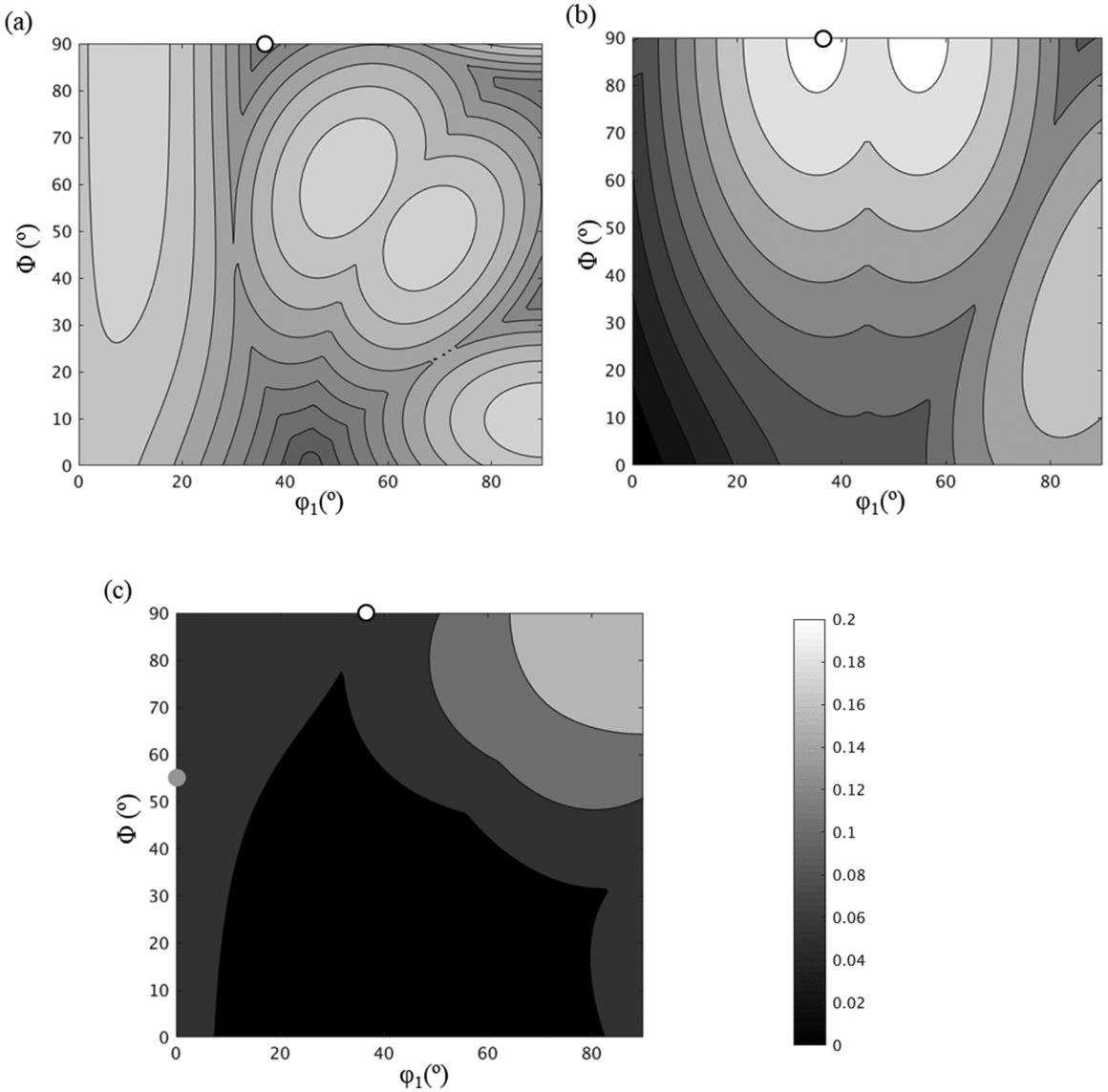

Fig. 13. Orientation distribution plots of non-dimensional mechanical driving force for austenite-to-ε martensite transformation on the section of $\varphi_2 = 45^\circ$ for (a) uniaxial tension, (b) pure shear, and (c) uniaxial compression. The orientations of longitudinal specimens are marked with open symbols at (35°, 90°, 45°). The orientation of the transverse specimen is marked with a solid symbol at (0°, 55°, 45°).

Table 3
Non-dimensional mechanical driving forces for martensitic transformation for the stress states studied.

		Mechanical driving force for austenite-to-α' martensite transformation	Mechanical driving force for austenite-to-ε martensite transformation
Uniaxial tension	Longitudinal	0.035	0.11
Pure shear	–	0.086	0.20
Uniaxial compression	Longitudinal	0.019	0.056
	Transverse	0.020	0.083

triaxiality, η, and Lode angle parameter, $\bar{\theta}$. Stress triaxiality, η, is defined as:

$$\eta = \frac{\sigma_m}{\sigma_{vM}} \tag{11}$$

where σ_m is the hydrostatic stress, which is proportional to the first invariant, I_1, of stress tensor, $\boldsymbol{\sigma}$, and σ_{vM} is the von Mises equivalent stress, which is a function of the second invariant, J_2, of the deviatoric stress tensor, $\boldsymbol{s}$, given as:

$$\sigma_m = \frac{1}{3}I_1 = \frac{1}{3}tr(\boldsymbol{\sigma}) \text{ and } \sigma_{vM} = \sqrt{3J_2} = \sqrt{\frac{3}{2}\boldsymbol{s}:\boldsymbol{s}} \tag{12}$$

The Lode angle parameter, $\bar{\theta}$, is a function of the second and third invariants of the deviatoric stress tensor, J_2 and J_3, and is given as:

$$\bar{\theta} = 1 - \frac{2}{\pi}\arccos\left(\frac{3\sqrt{3}}{2}\frac{J_3}{\sqrt{J_2^3}}\right) \text{ and } J_3 = det(\boldsymbol{s}). \tag{13}$$

The material parameter D in Eq. (10) may be expressed as a function of stress triaxiality and Lode angle parameter as [24]:

$$D = D_0 + a_\eta \eta + a_{\bar{\theta}} \bar{\theta} \quad (14)$$

where D_0, a_η, and a_θ are material parameters; and a_η and a_θ describe the contributions of stress triaxiality and Lode angle parameter to phase transformation.

The stress state-dependent strain-induced martensitic transformation kinetics equation proposed by Beese and Mohr [24] is chosen as a starting point for additively manufactured, or textured, SS304L. The effect of chemistry on transformation kinetics is considered through its impact on c_{max} and n, whose dependence on chemistry for this material was defined and calibrated in [51]. The equation proposed by Beese and Mohr [24] describes the transformation rate in terms of stress triaxiality and Lode angle parameter. The equation, calibrated in their study for a texture-free austenitic stainless steel, captured the fact that material loaded under uniaxial tension had the highest transformation rate, followed by that loaded under pure shear and uniaxial compression in that material. These trends were explained by the fact that the tensile normal stress acting on the maximum shear plane, which aids strain-induced martensitic transformation [20], increases with stress triaxiality and Lode angle parameter in an untextured material [24]. In contrast to the nearly isotropic material with equiaxed grains studied in [24], this study investigates materials with elongated grains with preferred crystallographic texture, requiring a new transformation kinetics equation that incorporates the effect of texture.

4.4.2. Proposed strain-induced martensitic transformation kinetics equation

As shown in Fig. 9, the rate of strain-induced martensitic transformation with respect to plastic strain in the present study from high to low is: uniaxial compression, uniaxial tension, and pure shear. The anomaly in the present data compared to data for isotropic stainless steel may result from the combined effects of stress state and texture. In order to capture the effect of texture, Eq. (14) is modified to give:

$$D = D_0 + a_\eta \eta + a_{\theta 1} \bar{\theta} + a_{\theta 2} \bar{\theta}^2 + a_W W \quad (15)$$

where $a_{\theta 1}$ and $a_{\theta 2}$ describe the contributions of Lode angle parameter to phase transformation; W is the non-dimensional mechanical driving force for austenite-to-α' martensite phase transformation, which depends on texture and applied stress; and the constant a_W describes the effect of W on the rate of phase transformation. Here, a first approximation is made that the impacts of stress state and preferred crystallographic texture can be considered independently and added together. Further work, beyond the scope of this study, is required to further investigate and fully justify this approximation; however, the goal here is to provide a framework for describing the experimentally observed coupling between stress state and texture. Furthermore, the calibrated value of a_W applies only to the longitudinal samples with the preferred texture observed here. The calibrated value of a_W would change with increased or decreased texture, and its purpose is simply to describe the enhancement or muting of phase transformation due to any crystallographic preferred texture.

The initial values of stress triaxiality, η, and Lode angle parameter, $\bar{\theta}$, for the tests performed in the present study are given in Table 4. The parameters, D_0, a_η, $a_{\theta 1}$, $a_{\theta 2}$, and a_W were calibrated using experimentally measured curves under uniaxial tension, pure shear, and uniaxial compression from the 80% and 90% SS304L walls, with the calibrated values given in Table 5. As shown in Fig. 9, the calibrated transformation kinetics equation is able to capture the experimentally measured strain-induced martensite evolution as a function of plastic strain, texture, stress state, and chemistry.

Table 4
Initial stress triaxiality, η, and Lode angle parameter, $\bar{\theta}$, for the stress states studied.

	Uniaxial tension	Pure shear	Uniaxial compression
η	0.33	0	−0.33
$\bar{\theta}$	1	0	−1

Table 5
Calibrated parameters for the strain-induced phase transformation kinetics equation for the 80% and 90% SS304L walls.

	D_0	a_η	$a_{\theta 1}$	$a_{\theta 2}$	a_W	D
Uniaxial tension	2.7	3.0	−1.8	1.4	1.6	3.4
Pure shear	2.7	3.0	−1.8	1.4	1.6	2.8
Uniaxial compression	2.7	3.0	−1.8	1.4	1.6	4.9

The existing transformation kinetics equations in previous studies only consider the effect of stress state, texture, or chemistry on strain-induced martensitic transformation independently [22–24,41,51,56,86]. However, the newly proposed transformation kinetics equation, calibrated using data under uniaxial tension, uniaxial compression, and pure shear for the textured SS304L in the present study, successfully combines the effects of stress state, chemistry, and texture together. Explicit consideration of the combined effects of these factors is necessary to describe microstructural evolution in additively manufactured austenitic stainless steels.

5. Summary and conclusions

Two 304L stainless steel walls with different initial powder compositions were fabricated using DED AM and subjected to mechanical loading (uniaxial tension, uniaxial compression, and pure shear) to investigate the effects of stress state and chemistry on strain-induced martensitic phase transformation in samples with preferred crystallographic texture. The primary findings of this work include:

- In both additively manufactured SS304L walls studied here, the rate of strain-induced martensitic transformation with respect to plastic strain was highest under uniaxial compression, followed by uniaxial tension, and lowest under pure shear. This result contradicts most of the reported findings of stress state-dependent strain-induced martensitic transformation in texture-free materials, which may be due to the combined effects of stress state and preferred crystallographic texture in the current materials.
- The strain-induced martensitic transformation kinetics also depend strongly on chemistry. Under the same stress state, the additively manufactured SS304L wall with a lower austenite stability (higher volume fraction of iron) had a higher rate of strain-induced martensitic transformation (with respect to plastic strain), and a higher saturation value of strain-induced martensite volume fraction.
- Based on the experimental findings of this study, a stress state-, texture-, and chemistry-dependent strain-induced martensitic transformation kinetics equation is proposed for SS304L. In a single wall, in addition to stress state itself (defined by stress triaxiality and Lode angle parameter), the rate of strain-induced martensitic transformation with respect to plastic strain depends on the driving force for austenite-to-α' martensite transformation, which depends on the combined effects of stress state and crystallographic texture. The newly proposed transformation kinetics equation is able to capture the combined effects of stress state, texture, and chemistry on the strain-induced phase transformation. A model of the microstructural evolution with these factors and plastic strain is used for the development of a physically-based plasticity model described in the companion paper [59], which captures the constitutive behavior of textured austenitic stainless steels.

Acknowledgments

The authors gratefully acknowledge the financial support provided by the National Science Foundation through award numbers CMMI-

1402978 and CMMI-1652575. Any opinions, findings, and conclusions or recommendations in the materials are those of the authors and do not necessarily reflect the views of the Nation Science Foundation. We thank Dr. Dong Ma and Mr. Matthew Frost of ORNL for neutron diffraction data collection and technical support at the VULCAN beamline, Dr. Alexandru D. Stoica of ORNL for Rietveld refinement analysis, Dr. Pierre-Olivier Santacreu for magnetic saturation measurements, and Dr. Adam Creuziger of NIST for valuable discussions.

Data availability

All relevant data are available from the authors.

References

[1] D.D. Gu, W. Meiners, K. Wissenbach, R. Poprawe, Laser additive manufacturing of metallic components: materials, processes and mechanisms, Int. Mater. Rev. 57 (2012) 133–164, https://doi.org/10.1179/1743280411Y.0000000014.
[2] X. Wu, A review of laser fabrication of metallic engineering components and of materials, Mater. Sci. Technol. 23 (2007) 631–640, https://doi.org/10.1179/174328407×179593.
[3] ASTM F2792: Standard terminology for additive manufacturing technologies, ASTM International, West Conshohocken, PA, 2012. ⟨http://dx.doi.org/10.1520/F2792-12A.2⟩.
[4] D.D. Gu, W. Meiners, K. Wissenbach, R. Poprawe, Laser additive manufacturing of metallic components: materials, processes and mechanisms, Int. Mater. Rev. 57 (2012) 133–164, https://doi.org/10.1179/1743280411Y.0000000014.
[5] W. Gao, Y. Zhang, D. Ramanujan, K. Ramani, Y. Chen, C.B. Williams, C.C.L. Wang, Y.C. Shin, S. Zhang, P.D. Zavattieri, The status, challenges, and future of additive manufacturing in engineering, Comput. Des. 69 (2015) 65–89, https://doi.org/10.1016/j.cad.2015.04.001.
[6] Z. Wang, A.D. Stoica, D. Ma, A.M. Beese, Diffraction and single-crystal elastic constants of Inconel 625 at room and elevated temperatures determined by neutron diffraction, Mater. Sci. Eng. A 674 (2016) 406–412, https://doi.org/10.1016/j.msea.2016.08.010.
[7] T. DebRoy, H.L. Wei, J.S. Zuback, T. Mukherjee, J.W. Elmer, J.O. Milewski, A.M. Beese, A. Wilson-Heid, A. De, W. Zhang, Additive manufacturing of metallic components – process, structure and properties, Prog. Mater. Sci. 92 (2018) 112–224, https://doi.org/10.1016/j.pmatsci.2017.10.001.
[8] Z. Wang, A.D. Stoica, D. Ma, A.M. Beese, Stress relaxation in a nickel-base superalloy at elevated temperatures via in situ neutron diffraction characterization: application to additive manufacturing, Mater. Sci. Eng. A 714 (2018) 75–83, https://doi.org/10.1016/j.msea.2017.09.071.
[9] Z. Wang, A.D. Stoica, D. Ma, A.M. Beese, Stress relaxation behavior and mechanisms in Ti-6Al-4V determined via in situ neutron diffraction: application to additive manufacturing, Mater. Sci. Eng. A 707 (2017) 585–592, https://doi.org/10.1016/j.msea.2017.09.071.
[10] K. Zhang, S. Wang, W. Liu, X. Shang, Characterization of stainless steel parts by laser metal deposition shaping, Mater. Des. 55 (2014) 104–119, https://doi.org/10.1016/j.matdes.2013.09.006.
[11] B.E. Carroll, T.A. Palmer, A.M. Beese, Anisotropic tensile behavior of Ti–6Al–4V components fabricated with directed energy deposition additive manufacturing, Acta Mater. 87 (2015) 309–320, https://doi.org/10.1016/j.actamat.2014.12.054.
[12] B. AlMangour, J.M. Yang, Understanding the deformation behavior of 17-4 precipitate hardenable stainless steel produced by direct metal laser sintering using micropillar compression and TEM, Int. J. Adv. Manuf. Technol. 90 (2017) 119–126, https://doi.org/10.1007/s00170-016-9367-9.
[13] I. Tolosa, F. Garciandía, F. Zubiri, F. Zapirain, A. Esnaola, Study of mechanical properties of AISI 316 stainless steel processed by “selective laser melting”, following different manufacturing strategies, Int. J. Adv. Manuf. Technol. 51 (2010) 639–647, https://doi.org/10.1007/s00170-010-2631-5.
[14] M.L. Griffith, D.M. Keicher, C.L. Atwood, J.A. Romero, E. Smugeresky, L.D. Harwell, D.L. Greene, Free form fabrication of metallic components using laser engineered net shaping (LENS), Proc. Solid Free. Fabr. Symp. (1996) 125–132.
[15] J. Yu, M. Rombouts, G. Maes, Cracking behavior and mechanical properties of austenitic stainless steel parts produced by laser metal deposition, Mater. Des. 45 (2013) 228–235, https://doi.org/10.1016/j.matdes.2012.08.078.
[16] M. Ma, Z. Wang, D. Wang, X. Zeng, Control of shape and performance for direct laser fabrication of precision large-scale metal parts with 316L stainless Steel, Opt. Laser Technol. 45 (2013) 209–216, https://doi.org/10.1016/j.optlastec.2012.07.002.
[17] A.E. Wilson-Heid, Z. Wang, B. McCornac, A.M. Beese, Quantitative relationship between anisotropic strain to failure and grain morphology in additively manufactured Ti-6Al-4V, Mater. Sci. Eng. A 706 (2017) 287–294, https://doi.org/10.1016/j.msea.2017.09.017.
[18] F. Lecroise, A. Pineau, Martensitic transformations induced by plastic-deformation in Fe-Ni-Cr-C system, Metall. Trans. 3 (1972) 387–396.
[19] T. Angel, Formation of martensite in austenitic stainless steels, effect of deformation, temperature and composition, J. Iron Steel Inst. (1954) 165–174.
[20] J.R. Patel, M. Cohen, Criterion for the action of applied stress in the martensitic transformation, Acta Metall. 1 (1953) 531–538, https://doi.org/10.1016/0001-6160(53)90083-2.
[21] G.B. Olson, M. Cohen, A mechanism for the strain-induced nucleation of martensitic transformations, J. Less- Common Met. 28 (1972) 107–118.
[22] R.G. Stringfellow, D.M. Parks, G.B. Olson, A constitutive model for transformation plasticity accompanying strain-induced martensitic transformations in metastable austenitic steels, Acta Metall. Mater. 40 (1992) 1703–1716, https://doi.org/10.1016/0956-7151(92)90114-T.
[23] G.B. Olson, M. Cohen, Kinetics of strain-induced martensitic nucleation, Metall. Trans. A 6 (1975) 791–795, https://doi.org/10.1007/BF02672301.
[24] A.M. Beese, D. Mohr, Effect of stress triaxiality and Lode angle on the kinetics of strain-induced austenite-to-martensite transformation, Acta Mater. 59 (2011) 2589–2600 ⟨http://linkinghub.elsevier.com/retrieve/pii/S1359645410008724⟩.
[25] J.B. Leblond, Mathematical modelling of transformation plasticity in steels II: coupling with strain hardening phenomena, Int. J. Plast. 5 (1989) 573–591, https://doi.org/10.1016/0749-6419(89)90002-8.
[26] R.G. Stringfellow, D.M. Parks, A self-consistent model of isotropic viscoplastic behavior in multiphase materials, Int. J. Plast. 7 (1991) 529–547.
[27] A.M. Beese, D. Mohr, Anisotropic plasticity model coupled with Lode angle dependent strain-induced transformation kinetics law, J. Mech. Phys. Solids 60 (2012) 1922–1940, https://doi.org/10.1016/j.jmps.2012.06.009.
[28] G.W. Greenwood, R.H. John, The deformation of metals under small stresses during phase transformations, Proc. R. Soc. Lond. A Math. Phys. Sci. 283 (1965) 403–422.
[29] H.K.D.H. Bhadeshia, Worked Examples in the Geometry of Crystals, Second ed., Londin, 2001. ⟨http://dx.doi.org/10.1524/zkri.1991.195.1-2.155⟩.
[30] A. Creuziger, W.A. Poling, T. Gnaeupel-herold, A. Creuziger, W.A. Poling, Assessment of Martensitic Transformation Paths Based on Transformation Potential Calculations, Steel Research International, In press (2018).
[31] J. Talonen, Effect of Strain-induced α'-Martensite Transformation on Mechanical Properties of Metastable Austenitic Stainless Steels, Helsinki University of Technology, 2007.
[32] L. Facchini, N. Vicente, I. Lonardelli, E. Magalini, P. Robotti, M. Alberto, Metastable austenite in 17-4 precipitation-hardening stainless steel produced by selective laser melting, Adv. Eng. Mater. 12 (2010) 184–188, https://doi.org/10.1002/adem.200900259.
[33] D. Kaoumi, J. Liu, Deformation induced martensitic transformation in 304 austenitic stainless steel: in-situ vs. ex-situ transmission electron microscopy characterization, Mater. Sci. Eng. A 715 (2018) 73–82, https://doi.org/10.1016/j.msea.2017.12.036.
[34] B. Cina, Effect of cold work on the γ → α transformation in some Fe-Ni-Cr alloys, J. Iron Steel Inst. 177 (1954) 406.
[35] P. Hilkhuijsen, H.J.M. Geijselaers, T.C. Bor, E.S. Perdahcioğlu, A.H. vd Boogaard, R. Akkerman, Strain direction dependency of martensitic transformation in austenitic stainless steels: the effect of γ-texture, Mater. Sci. Eng. A 573 (2013) 100–105, https://doi.org/10.1016/j.msea.2013.02.036.
[36] P. Hilkhuijsen, H.J.M. Geijselaers, T.C. Bor, The influence of austenite texture on the martensitic transformation of an austenitic stainless steel, J. Alloy. Compd. 577 (2013) 609–613, https://doi.org/10.1016/j.jallcom.2012.02.147.
[37] D. De Knijf, T. Nguyen-Minh, R.H. Petrov, L.A.I. Kestens, J.J. Jonas, Orientation dependence of the martensite transformation in a quenched and partitioned steel subjected to uniaxial tension, J. Appl. Crystallogr. 47 (2014) 1261–1266, https://doi.org/10.1107/S1600576714011959.
[38] G.W. Powell, E.R. Marshall, W.A. Backofen, Strain hardening of austenitic stainless steel, Trans. ASM 50 (1958) 478–497.
[39] S.S. Hecker, M.G. Stout, K.P. Staudhammer, J.L. Smith, Effects of strain state and strain rate on deformation- induced transformation in 304 stainless steel part I. Magnetic measurements and mechanical behavior, Metall. Trans. 13A (1982) 619–626.
[40] L.E. Murr, K.P. Staudhammer, S.S. Hecker, Effects of strain state and strain rate on deformation-induced transformation in 304 stainless steel: part II. Microstructural study, Metall. Trans. A 13A (1982) 627–635.
[41] V.V. Kosarchuk, L.V. Zaitseva, A.A. Lebedev, B.I. Koval'chuk, Effect of stressed state parameters on phase transformation kinetics in austenitic steels with plastic deformation, Strength Mater. 21 (1989) 60–64, https://doi.org/10.1017/CBO9781107415324.004.
[42] T. Iwamoto, T. Tsuta, Y. Tomita, Investigation on deformation mode dependence of strain-induced martensitic transformation in trip steels and modelling of transformation kinetics, Int. J. Mech. Sci. 40 (1998) 173–182, https://doi.org/10.1016/S0020-7403(97)00047-7.
[43] H.Y. Yu, Y.K. Gao, D.J. Meng, Transformation behavior of retained austenite under different deformation modes for low alloyed TRIP-assisted steels, Mater. Sci. Eng. A 441 (2006) 331–335, https://doi.org/10.1016/j.msea.2006.08.061.
[44] H. Kim, J. Lee, F. Barlat, D. Kim, M.G. Lee, Experiment and modeling to investigate the effect of stress state, strain and temperature on martensitic phase transformation in TRIP-assisted steel, Acta Mater. 97 (2015) 435–444, https://doi.org/10.1016/j.actamat.2015.06.023.
[45] A. Creuziger, T. Foecke, Transformation potential predictions for the stress-induced austenite to martensite transformation in steel, Acta Mater. 58 (2010) 85–91, https://doi.org/10.1016/j.actamat.2009.08.059.
[46] R.E. Schramm, R.P. Reed, Stacking fault energies of seven commercial austenitic stainless steels, Metall. Trans. A 6A (1975) 1345–1351, https://doi.org/10.1007/BF02641927.
[47] K. Tomimura, S. Takaki, S. Tanimoto, Y. Tokunaga, Optimal refining chemical composition in Fe-Cr-Ni alloys for ultra grain by reversion from deformation induced martensite, ISIJ Int. 31 (1991) 721–727.
[48] J. Talonen, H. Hänninen, Formation of shear bands and strain-induced martensite during plastic deformation of metastable austenitic stainless steels, Acta Mater. 55

(2007) 6108–6118, https://doi.org/10.1016/j.actamat.2007.07.015.
[49] H.K. Rafi, D. Pal, N. Patil, T.L. Starr, B.E. Stucker, Microstructure and mechanical behavior of 17-4 precipitation hardenable steel processed by selective laser melting, J. Mater. Eng. Perform. 23 (2014) 4421–4428, https://doi.org/10.1007/s11665-014-1226-y.
[50] Z. Wang, T.A. Palmer, A.M. Beese, Effect of processing parameters on microstructure and tensile properties of austenitic stainless steel 304L made by directed energy deposition additive manufacturing, Acta Mater. 110 (2016) 226–235, https://doi.org/10.1016/j.actamat.2016.03.019.
[51] Z. Wang, A.M. Beese, Effect of chemistry on martensitic phase transformation kinetics and resulting properties of additively manufactured stainless steel, Acta Mater. 131 (2017) 410–422.
[52] H.L. Wei, J. Mazumder, T. DebRoy, Evolution of solidification texture during additive manufacturing, Sci. Rep. 5 (2015) 1–7, https://doi.org/10.1038/srep16446.
[53] D. Ma, A.D. Stoica, Z. Wang, A.M. Beese, Crystallographic texture in an additively manufactured nickel-base superalloy, Mater. Sci. Eng. A 684 (2017) 47–53.
[54] G. Han, H. Yuan, Deformations and damage evolution of austenitic steel AISI304 with martensite phase transformation, in: Proceedings of the 13th International Conference Fracture, Beijing, 2013, pp. 1–11.
[55] C.-C. Young, Transformation Toughening of Phosphocarbide-Strengthened Austenitic Steels, Massachusetts Institute of Technology, 1988.
[56] A.A. Lebedev, V.V. Kosarchuk, Influence of phase transformations on the mechanical properties of austenitic stainless steels, Int. J. Plast. 16 (2000) 749–767, https://doi.org/10.1016/S0749-6419(99)00085-6.
[57] T. Okutani, N. Yukawa, K. Ishikawa, T. Jinma, The strain-induced martensitic transformation of SU304 under various stress states. Proc. Japanese Soc. Tech. Plast., 95 Spring, 1995, pp. 331–332.
[58] Y. Tomita, T. Iwamoto, Constitutive modeling of trip steel and its application to the improvement of mechanical properties, Int. J. Mech. Sci. 37 (1995) 1295–1305, https://doi.org/10.1016/0020-7403(95)00039-Z.
[59] Z. Wang, A.M. Beese, Stress state-dependent mechanics of additively manufactured 304L stainless steel: Part 2 - characterization and modeling of macroscopic plasticity behavior, Mater. Sci. Eng. A (2018), https://doi.org/10.1016/j.msea.2018.11.091 [article in press].
[60] ASTM A479/A479M: Standard specification for stainless steel bars and shapes for use in boilers and other pressure vessels, ASTM International, West Conshohocken, PA, 2018. ⟨http://dx.doi.org/10.1520/A0479_A0479M-18⟩.
[61] ASTM Standard E8/E8M-16a: Standard test methods for tension test of metallic materials, ASTM International, West Conshohocken, PA, 2016. ⟨http://dx.doi.org/10.1520/E0008_E0008M-16A⟩.
[62] R.J. Moat, A.J. Pinkerton, L. Li, P.J. Withers, M. Preuss, Residual stresses in laser direct metal deposited Waspaloy, Mater. Sci. Eng. A 528 (2011) 2288–2298, https://doi.org/10.1016/j.msea.2010.12.010.
[63] T. LeBrun, T. Nakamoto, K. Horikawa, H. Kobayashi, Effect of retained austenite on subsequent thermal processing and resultant mechanical properties of selective laser melted 17-4 PH stainless steel, Mater. Des. 81 (2015) 44–53, https://doi.org/10.1016/j.matdes.2015.05.026.
[64] S.S.M. Tavares, D. Gunderov, V. Stolyarov, J.M. Neto, Phase transformation induced by severe plastic deformation in the AISI 304L stainless steel, Mater. Sci. Eng. A 358 (2003) 32–36, https://doi.org/10.1016/S0921-5093(03)00263-6.
[65] R.D.K. Misra, B.R. Kumar, M. Somani, P. Karjalainen, Deformation processes during tensile straining of ultrafine/nanograined structures formed by reversion in metastable austenitic steels, Scr. Mater. 59 (2008) 79–82, https://doi.org/10.1016/j.scriptamat.2008.02.028.
[66] E. Villari, Change of magnetization be tension and by electric current, Ann. Phys. Chem. 126 (1865) 87–122.
[67] A.M. Beese, D. Mohr, Identification of the direction-dependency of the martensitic transformation in stainless steel using in situ magnetic permeability measurements, Exp. Mech. 51 (2011) 667–676, https://doi.org/10.1007/s11340-010-9374-y.
[68] P. Reu, Virtual strain gage size study, Exp. Tech. 39 (2015) 1–3.
[69] Fischer, Operator's Manual for Feritescope FMP30 Manual. 2008.
[70] D. Mohr, M. Oswald, A new experimental technique for the multi-axial testing of advanced high strength steel sheets, Exp. Mech. 48 (2008) 65–77, https://doi.org/10.1007/s11340-007-9053-9.
[71] K. An, H.D. Skorpenske, A.D. Stoica, D. Ma, X.L. Wang, E. Cakmak, First in situ lattice strains measurements under load at VULCAN, Metall. Mater. Trans. A Phys. Metall. Mater. Sci. 42 (2011) 95–99, https://doi.org/10.1007/s11661-010-0495-9.
[72] T. Ungar, A.D. Stoica, G. Tichy, X.-L. Wang, Orientation-dependent evolution of the dislocation density in grain populations with different crystallographic orientations relative to the tensile axis in a polycrystalline aggregate of stainless steel, Acta Mater. 66 (2014) 251–261, https://doi.org/10.1016/j.actamat.2013.11.012.
[73] G.M. Stoica, A.D. Stoica, M.K. Miller, D. Ma, Temperature-dependent elastic anisotropy and mesoscale deformation in a nanostructured ferritic alloy, Nat. Commun. 5 (2014) 1–8, https://doi.org/10.1038/ncomms6178.
[74] R.L. Snyder, The use of reference intensity ratios in x-ray quantitative analysis, Powder Diffr. 7 (1992) 186–193, https://doi.org/10.1017/S0885715600018686.
[75] H.M. Rietveld, A profile refinement method for nuclear and magnetic structures, J. Appl. Crystallogr. 2 (1969) 65–71.
[76] A.C. Larson, R.B. Von Dreele, General Structure Analysis System (GSAS), (2004).
[77] K. Mumtaz, S. Takahashi, J. Echigoya, Y. Kamada, L.F. Zhang, H. Kikuchi, K. Ara, M. Sato, Magnetic measurements of martensitic transformation in austenitic stainless steel after room temperature rolling, J. Mater. Sci. 39 (2004) 85–97, https://doi.org/10.1023/B:JMSC.0000007731.38154.e1.
[78] G.M. Stoica, A.D. Stoica, K. An, D. Ma, S.C. Vogel, J.S. Carpenter, X.L. Wang, Extracting grain-orientation-dependent data from in situ time-of-flight neutron diffraction. I. Inverse pole figures, J. Appl. Crystallogr. 47 (2014) 2019–2029, https://doi.org/10.1107/S1600576714023036.
[79] ASTM E1019: Standard test methods for determination of carbon, sulfur, nitrogen, and oxygen in steel and in iron, nickel, and cobalt alloys by various combustion and fusion techniques, ASTM International, West Conshohocken, PA, 2015. ⟨http://dx.doi.org/10.1520/E1019-11⟩.
[80] ASTM E1086: Standard test method for analysis of austenitic stainless steel by spark atomic emission spectrometry, ASTM International, West Conshohocken, PA, 2015. ⟨http://dx.doi.org/10.1520/E1086-14.2⟩.
[81] ASTM Standard E975-13: Standard practice for X-ray determination of retained austenite in near random crystallographic orientation, ASTM International, West Conshohocken, PA, 2013. ⟨http://dx.doi.org/10.1520/E0975-13⟩.
[82] A.M. Beese, Z. Wang, A.D. Stoica, D. Ma, Absence of dynamic strain aging in an additively manufactured nickel-base superalloy, Nat. Commun. 9 (2018) 2083.
[83] M.S. Wechsler, D.S. Lieberman, T.A. Read, On the theory of the formation of martensite, Trans. AIME (1953) 1503–1515.
[84] M. Humbert, B. Petit, B. Bolle, N. Gey, Analysis of the γ–ε–α′ variant selection induced by 10% plastic deformation in 304 stainless steel at −60 °C, Mater. Sci. Eng. A 454–455 (2007) 508–517.
[85] T.W. Shield, Orientation dependence of the pseudoelastic behavior of single crystals of CuAlNi in tension, J. Mech. Phys. Solids 43 (1995) 869–895, https://doi.org/10.1016/0022-5096(95)00011-7.
[86] P.O. Santacreu, J.C. Glez, G. Chinouilh, T. Frohlich, Behaviour model of austenitic stainless steels for automotive structural parts, Steel Res. Int. 77 (2006) 686–691.
[87] D. DeMania, The Influence of Martensitic Transformation on the Formability of 304L Stainless Steel Sheet, Massachusetts Institue of Technology, 1995.
[88] M.P. Miller, D.L. McDowell, The effect of stress state on the large strain inelastic deformation behavior of 304L stainless steel, J. Eng. Mater. Technol. 118 (1996) 28–36.
[89] H.C. Shin, T.K. Ha, W.J. Park, Y.W. Chang, Deformation-induced martensitic transformation under various deformation modes, Key Eng. Mater. 233–236 (2003) 667–672, https://doi.org/10.4028/www.scientific.net/KEM.233-236.667.
[90] E.S. Perdahcioglu, H.J.M. Geijselaers, J. Huétink, Influence of stress state and strain path on deformation induced martensitic transformations, Mater. Sci. Eng. A 481–482 (2008) 727–731, https://doi.org/10.1016/j.msea.2007.02.153.
[91] S. Nanga, A. Pineau, B. Tanguy, L. Naze, P.O. Santacreu, Plasticity and strain induced martensitic transformation in two austenitic stainless steels, in: Proceedings International Conference Martensitic Transform., New Mexico, 2009, pp. 341–348.